Available online at www.sciencedirect.com

ScienceDirect

Ceramics International 40 (2014) 1387–1397

CERAMICS INTERNATIONAL

www.elsevier.com/locate/ceramint

Mesoporous vanadium oxide nanostructures: Hydrothermal synthesis, optical and electrochemical properties

I. Mjejri[a], N. Etteyeb[a], F. Sediri[a,b,*]

[a]Laboratory of Condensed Matter Chemistry, IPEIT, University of Tunis 2, Jawaher Lel Nehru 1008, B. P. 229 Montfleury, Tunisia
[b]Chemistry Department, Sciences Faculty of Tunis, Tunis El Manar University, 2092 El Manar, Tunisia

Received 26 June 2013; accepted 3 July 2013
Available online 16 July 2013

Abstract

VO_2(B) nanoplates and nanorods have been successfully synthesized via a hydrothermal process by using V_2O_5 as vanadium source and HO–$(CH_2)_n$–OH (with $n=3$ and 5) as reducing and structure directing agents. The morphology, the structure, the crystallinity and the composition of the materials were investigated by X-ray diffraction (DRX), scanning electron microscopy (SEM), Raman spectroscopy, X-ray photoelectron spectroscopy (XPS) and nitrogen adsorption/desorption isotherms respectively have been used. The optical properties of the as-synthesized VO_2(B) were investigated by UV–visible absorption and photoluminescence. Electrochemical measurements have revealed reversible redox behavior with charge–discharge cycling corresponding to the reversible lithium intercalation/deintercalation.

Keywords: B. X-ray methods; C. Optical properties; D. Transition metal oxides

1. Introduction

One-dimensional (1D) nanostructures, such as nanobelts, nanorods, nanowires and nanotubes, have considerable interest due to their fundamental research importance and the wide range of their potential applications in nanodevices [1–7]. These materials have exhibited novel optical, electrical, magnetic, mechanical and energy conversional properties, which were different from those of bulk materials [8]. Among them, metal oxide nanostructured materials can exhibit unique chemical properties due to their limited size and a high density of corner or edge surface sites [9]. These properties make nanostructured metal oxides useful for a wide range of applications including lithium ion battery [10–14]. Vanadium oxides VO_x (V_2O_5, VO_2, V_2O_4, V_3O_7. H_2O, V_2O_3, V_6O_{13}) [15] are interesting electrode materials for lithium ion batteries because of its typical intercalation structure, low cost and tunable oxidation state (from +2 to +5). Among these, VO_2 and $V_3O_7 \cdot H_2O$ have attracted much attention due to its potential application in transistors, electrical and optical switch devices and lithium ion battery [16–18]. VO_2(B) is one of vanadium dioxide polymorphs [6]. Since the discovery of the metal-semiconductor transition in VO_2 by Morin [19], this new frontier attracts many eyes of different researchers. The motivation is that VO_2 can be used in different areas, such as temperature sensing devices, optical switching devices, modulator, and polarizer of sub-millimeter wave radiation, optical data storage medium, energy efficiency windows, etc. [20–21]. VO_2(B), with a metastable monoclinic structure, is a promising electrode material to be applied in lithium ion batteries, owing to not only its proper electrode potential but also its tunnel structure, through which lithium ions can make intercalation and deintercalation in reversible lithium-ion batteries [22]. And good capacity retention on cycling also makes it an attractive cathode for rechargeable lithium-ion batteries [23].

Several synthetic ways such as microemulsion-mediated systems, arc discharge, laser-assisted catalysis growth, solution, vapor transport, and solvothermal and hydrothermal methods have been successfully explored to fabricate various kinds of nanostructured vanadium oxides and their derived compounds. As one of the solution methods, the hydrothermal

*Coresponding author at: Chemistry Department, Sciences Faculty of Tunis, Tunis El Manar University, 2092 El Manar, Tunisia. Tel.: +216 71336641; fax: +216 71337323.
E-mail address: faouzi.sediri@ipeit.rnu.tn (F. Sediri).

0272-8842/$ - see front matter © 2013 Elsevier Ltd and Techna Group S.r.l. All rights reserved.
http://dx.doi.org/10.1016/j.ceramint.2013.07.020

method has been extensively used for the synthesis of inorganic compounds. Previously, various kinds of vanadium oxide nanostructures such as nanowires, nanobelts, nanorods, nanotubes, nanostructured foam, and nanoribbons have been reported [24–31]. In this paper, we described a simple one step hydrothermal route for the synthesis of VO_2(B) nanoplates and nanorods using HO–$(CH_2)_n$–OH with n=3 and 5 as a reducing and structure-directing agents agent for the first time. The electroactivity of the VO_2(B) nanorods has been investigated. Cyclic voltammetric characterization of thin films of the nanostructured VO_2(B) has revealed reversible redox behavior with charge–discharge cycling corresponding to the reversible lithium intercalation/deintercalation into the crystal lattice of the VO_2(B). The as-synthesized nanoplates and nanorods exhibit good electrochemical behavior and promising to be used in lithium-ion battery.

2. Experimental section

2.1. Hydrothermal synthesis

All of the chemical reagents were purchased from Acros and used without further purification. Vanadium (V) oxide was used as vanadium source. The organics reagents, 1,3-propanediol and 1,5-pentanediol have been used as templates for the first time. VO_2(B) nanoplates and nanorods were hydrothermally synthesized, from a mixture of V_2O_5, HO–$(CH_2)_n$–OH (n=3 and 5) and distilled water (5 mL) in the molar ratio V/diol=1:1. Reactants were introduced in this order and stirred a few minutes before introducing the resulting suspension in a Teflon-lined steel autoclave and the temperature set at 180 °C for 2 days. The pH of the solution remains close to pH≈7 during the whole synthesis. The obtained black powder was washed with acetone to remove organics residues and then dried at 80 °C. The black color of the powder suggested that some V^{5+} ions had been reduced to V^{4+} by decomposition of the organic compound [32]. To investigate the formation process of VO_2(B) nanostructures, time dependent experiments were carried out at 180 °C.

2.2. Characterization techniques

X-ray powder diffraction data (XRD) were obtained on a X′ Pert Pro Panalytical diffractometer with CuKα radiation (λ=1.5418 Å) and graphite monochromator. The XRD measurements were carried out by applying a step scanning method (2θ range from 3° to 70°), the scanning rate is 0.017° s^{-1} and the step time is 1 s. Scanning electron microscopy (SEM) study was recorded on a Cambridge Instruments Stereoscan 120. Fourier-transform infrared spectra (FTIR) were recorded from 4000 to 400 cm^{-1} on a Nicolet 380 spectrometer in pellets of samples dispersed in KBr. Raman spectroscopy was performed using a Jobin Yvon T 64000 spectrometer (blue laser excitation with 488 nm wavelength and < 55 mW power at the sample). X-ray photoelectron spectroscopy (XPS) experiments were performed using a Shimadzu ESCALAB at room temperature. The Brunauer–Emmett–Teller (BET) specific surface area, average pore diameter and pore size distributions were determined by nitrogen physisorption at 77 K using a Micrometrics ASAP-2000 instrument. The optical parameters of sample were calculated from the optical absorbance data recorded in the wavelength range from 300 to 900 nm using a UV–visible spectrophotometer Shimadzu-3101PC. Photoluminescence (PL) spectroscopy was performed to investigate the optical properties of the samples using a 250 mm Jobin Yvon luminescence spectrometer. The electrochemical measurements were carried out using one compartment cell and a BioLogic SP150 potentiostat/galvanostat apparatus. Ag/AgCl electrode and a stainless grid were used as reference and counter-electrode electrode, respectively. The working electrode is a film of VO_2(B) deposited on a plate of indium tin oxide (ITO). The operating voltage was controlled between −0.4 V and 1.0 V at different scan rates. The electrolyte was the lithium perchlorate 1 M ($LiClO_4$) dissolving in propylene carbonate (PC). All measurements were performed at room temperature.

3. Results and discussion

3.1. X-ray diffraction

Powder X-ray diffraction patterns of the resulting samples synthesized with 1,3-propanediol at 180 °C for different

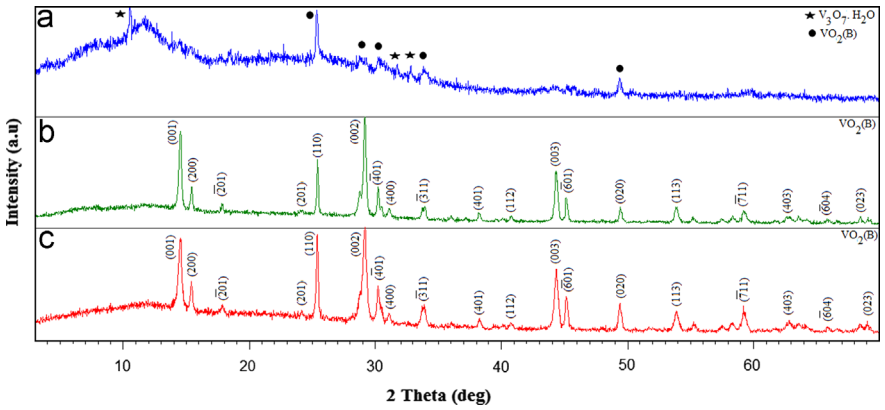

Fig. 1. XRD patterns of the samples synthesized with 1,3-propanediol at 180 °C for different reaction times: 1 day (a), 2 days (b) and 4 days (c).

reaction times: 1 day (a), 2 days (b) and 4 days (c), are shown in Fig. 1. It is obvious that the crystalline phases for vanadium oxide nanorods are discriminatory at different reaction times. Indeed, after a one day synthesis process (Fig. 1a), the diffraction pattern shows the presence of VO_2(B) (JCPDS card no. 31-1438) with the presence of a peaks which are characteristic of $V_3O_7 \cdot H_2O$ (JCPDS card no. 85-2401). All diffraction peaks can be perfectly indexed to the monoclinic VO_2(B) crystalline phase with lattice parameters $a=12.03$ Å $b=3.693$ Å, $c=6.42$ Å and $\beta=106.6^\circ$ according to JCPDS # 31-1438 when the reaction time is increased to 2 and 4 days (Figs. 1b and c). However, Fig. 2 shows the XRD patterns of the as-obtained samples with 1,5-pentanediol at 180 °C for different reaction time (1–4 days). Indeed, the diffraction pattern always shows the presence of VO_2(B) (JCPDS card no. 31-1438) and another phase which was identified as $V_3O_7 \cdot H_2O$ (JCPDS card no. 85-2401) when the synthesis was carried out for 1 day (Fig. 2a), while the monoclinic VO_2(B) (JCPDS card no. 31-1438) has been obtained when the reaction time = 2 and 4 days (Figs. 2b and c). No peaks of any other phases or impurities were observed from the XRD patterns, indicating that the monoclinic VO_2(B) crystalline phase with high purity could be obtained using the present synthetic process. In fact, strong and sharp diffraction peaks also indicate good crystallinity of the hydrothermal product. It could be concluded that the reaction time has a significant effect on the crystalline phase of monoclinic VO_2(B).

3.2. Scanning electronic microscopy

The morphology of synthesized materials was investigated by using the scanning electron microscopy (SEM). Fig. 3 shows SEM images of the samples synthesized with 1,3-propanediol at 180 °C for different reaction times (1–4 days). In fact, the reaction time plays an important role in controlling the morphologies of VO_2 nanostructures. It is clear that the morphology of the material synthesized for 1 day is quite different from those synthesized for 2 and 4 days. Indeed, nearly plate-like morphology and a few amounts of irregular particles were observed in the material, as shown in Fig. 3a. When the synthesis was carried out for 2 days, a large amount of regular VO_2 nanoplates which became predominant decorated by rod morphology were synthesized (Fig. 3b). An increase in the reaction time brings about a change in the morphology of products. In addition, when the synthesis was carried out for 2 days the observation by scanning electronic microscopy shows that the as obtained sample is made of a homogenous phase with particles uniformly sized which display plate-like morphology (Fig. 3c). It was found that the different structure-directing agents lead to the different morphologies of samples as shown in SEM micrographs (Fig. 4). Indeed, when 1,5 pentanediol was used as the structure-directing agent for 2 days, the synthesized VO_2(B) had a nearly rod morphology and a few amount of irregular particles of VO_2(B) (Fig. 4a). It is clear that the morphology of the material synthesized for 1 day is quite different from those synthesized for 2 and 4 days. In fact, it is observed in Figs. 4b and c that the as-obtained VO_2 is made of a homogenous phase with particles regularly sized and which display typical rod-like morphology with a width ranging from 50 nm to 80 nm and several micrometers in length. The synthesis parameters, such as reaction time played an important role in controlling the purity and morphology.

3.3. Infrared spectroscopy

The structure information was further provided by FTIR spectroscopy. It allows characterizing and evaluating the apparition and the disappearance of the chemical functions from the vibration modes of the liaisons of the molecules. Similar characteristics can be seen in the infrared spectra of the samples. Fig. 5 shows the FTIR spectra of the VO_2(B) nanoplates and nanorods prepared at 180 °C for 2 days using 1,3-propanediol and 1,5-pentanediol. The analysis of the spectra shows the existence of bands relating to the vanadium–oxygen stretching vibrations between 400 and 1100 cm^{-1}. Indeed, the situated band about 1002 cm^{-1} is attributed to the vanadyl V=O stretching vibration [32]. The shift in this band compared to that for V_2O_5 (1025 cm^{-1}) is consistent with the reduced state of vanadium in VO_2(B) [32]. However, the situated bands to 848 and 530 cm^{-1} are assigned to the in-plane and out-of-plane V–O–V vibrations of

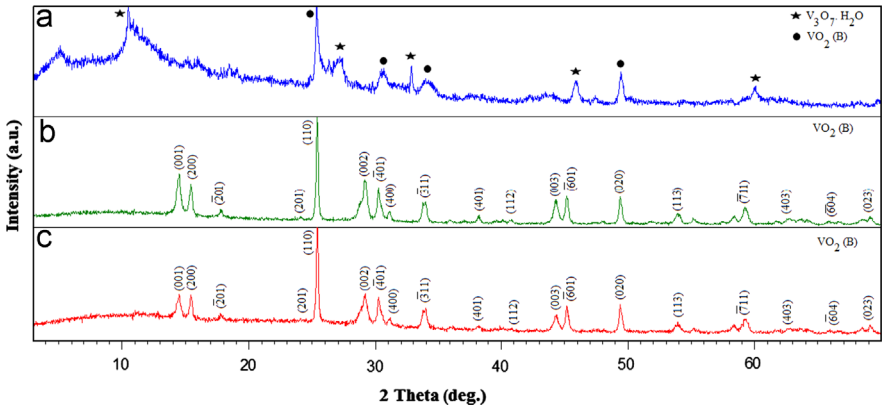

Fig. 2. XRD patterns of the samples synthesized with 1,5 pentanediol at 180 °C for different reaction times: 1 day (a), 2 days (b) and 4 days (c).

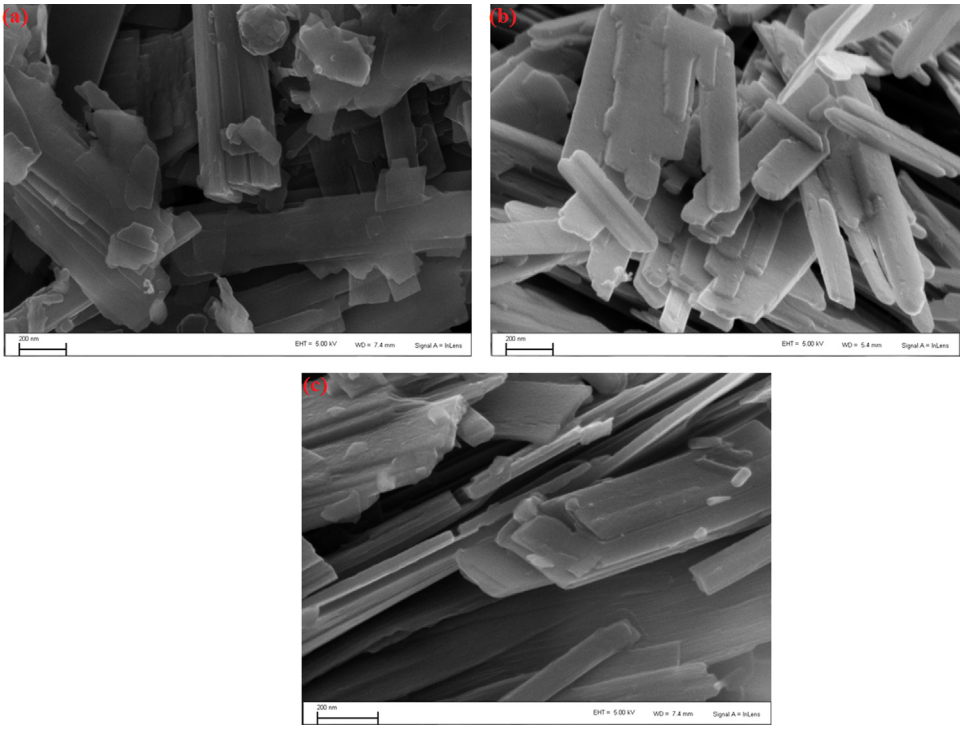

Fig. 3. SEM micrographs of the samples synthesized with 1,3-propanediol at 180 °C for different reaction times: 1 day (a), 2 days (b) and 4 days (c).

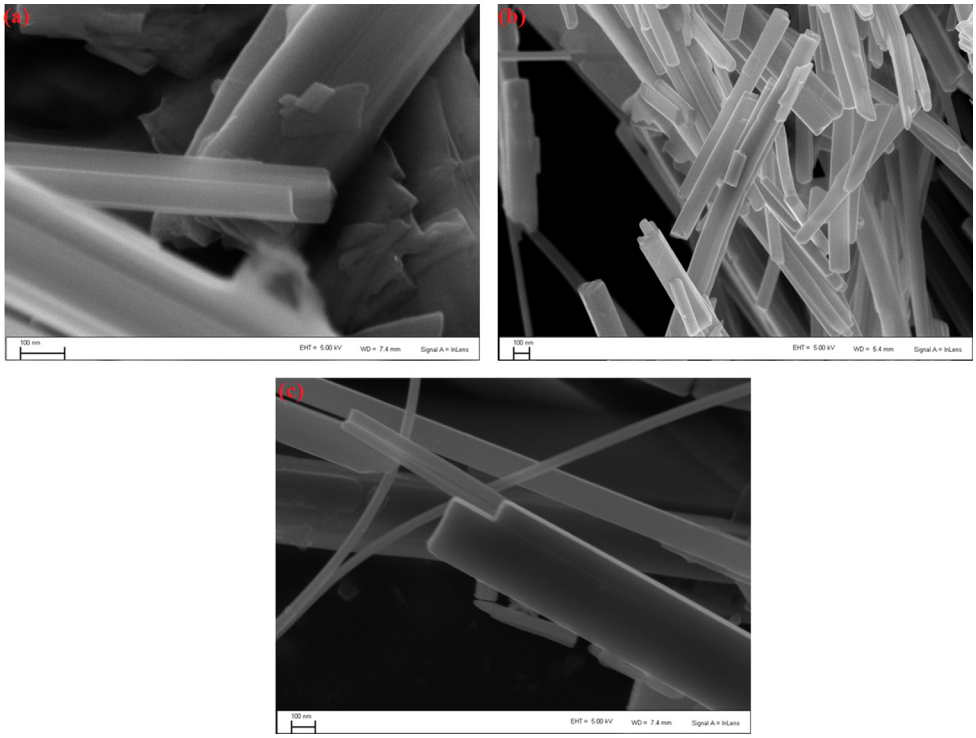

Fig. 4. SEM micrographs of the samples synthesized with 1,5 pentanediol at 180 °C for different reaction times: 1 day (a), 2 days (b) and 4 days (c).

deformation, respectively [33,34]. The stretching vibration and the bending vibration of water are seen at ca. 3436 cm^{-1} and ca. 1627 cm^{-1}, respectively, originating from the water adsorbed on the surface of the crystallites [35–37].

3.4. Raman spectroscopy

Raman spectroscopy was used to characterize this material since this technique is suitable to obtain details of the VO_2(B)

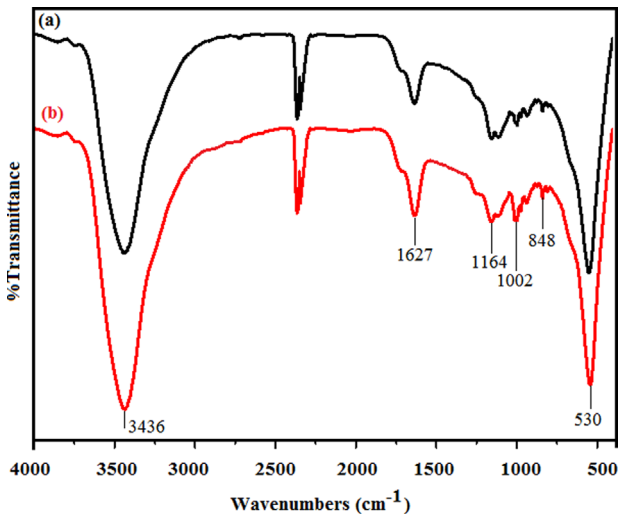

Fig. 5. IR spectra of the VO_2(B) nanoplates (a) and nanorods (b) synthesized for 2 days at 180 °C.

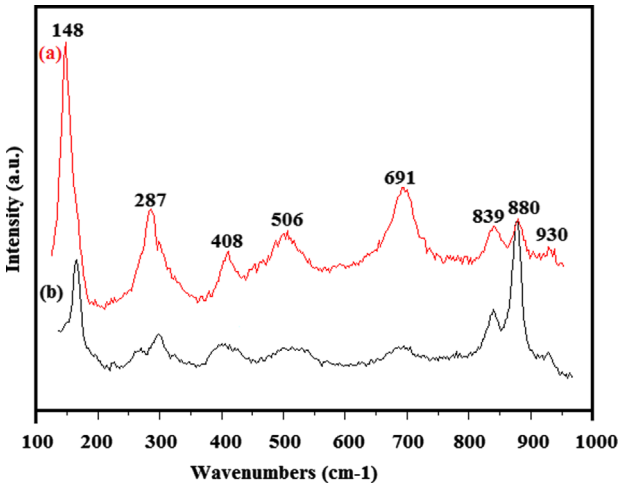

Fig. 6. Raman spectra of VO_2(B) nanoplates (a) and nanorods (b).

chemical structure. Raman spectra of the above samples are shown in Fig. 6. In fact, all samples showed similar Raman spectra. Indeed, the analysis of the spectra exhibits well defined bands centered at around 148, 287,408, 506, 691, 839, 880 and 930 cm^{-1}. According to the literature, these bands can be assigned to the fundamental modes of crystalline VO_2(B) monoclinic. The band at 148 cm^{-1} is attributed to the stretching mode of $(V_2O_2)_n$ which correspond to the chain translation [38–40]. The bands located at 408 and 287 cm^{-1} are assigned to the bending vibration of the V═O bonds [41]. The band at 506 cm^{-1} is attributed to the triply-coordinated oxygen (V_3–O) stretching mode [37]. The band at 691 cm^{-1} is assigned to the stretching vibration of the doubly coordinated oxygen (V_2–O) [42,43]. While the located bands at 839 and 880 cm^{-1} are assigned to the bending vibration of V–O–V groups involving doubly coordinated oxygen's. However, the high frequency Raman band situated at 930 cm^{-1} corresponds to the terminal oxygen (V═O) stretching mode which results from an unshared oxygen [44].

3.5. X-ray photoelectron spectroscopy (XPS)

The composition and vanadium valence state of the surface of the as-synthesized VO_2 (B) nanorods was further investigated by X-ray photoelectron spectroscopy (XPS), as shown in Fig. 7a, and the fitted-curves about $V2p_{3/2}$, $V2p_{1/2}$ and O1s are illustrated in Figs. 7b and c, respectively. The XPS survey spectrum (Fig. 7a) reveals that the sample only consists of vanadium and oxygen (the C1s peak was appeared, which could be due to some CO_2 absorbed on the surface of the sample). In fact, the peaks centered at 517.09, 524.12 and 530.84 eV are assigned to the $V2p_{3/2}$, $V2p_{1/2}$ and O1s, respectively. The $V2p_{3/2}$ peak of the sample is divided into two peaks at the binding energies of 517.46 and 516.97 eV (Fig. 7b), attributed to V^{4+} and V^{5+}, respectively [45–49]. The O1s core peak was divided into two peaks with the binding energies at 529.67 and 532.87 eV, attributed to O^{2-} and O^{-} species, respectively [47–50]. According to the analysis proposed by Chao-jun Cui et al. [50], superoxide ions O–is associated with the presence of V^{4+} ions. Quantification of the XPS peak areas gives that the surface ratio of V/O in the sample is about 0.6, which is very close to the chemical stoichiometry of V/O in the VO_2.

3.6. Optical properties

The optical properties of as-obtained VO_2(B) were studied by photoluminescence and UV–visible spectroscopy. The UV–visible spectra of VO_2(B) nanoplates and nanorods are shown in Fig. 8. It is well-known that the band maxima of the charge transfer transition of $O \rightarrow V^{n+}$ depends on the number of O atoms surrounding the central vanadium ion [51]. Therefore, V^{5+} in tetrahedral coordination absorbs in the range 240–350 nm, in square pyramidal coordination at 350–450 nm and in octahedral coordination at 450–600 nm [52,53]. In fact, the spectra exhibit a weak absorption band at around 320 nm which can be attributed to lower energy charge transfer to V^{5+} species in tetrahedral coordination. However the absorption band located at around 410 nm is attributable to the electron transfer from oxygen atoms to vanadium in square pyramidal coordination [54,55]. The optical band gap, Eg, can be estimated from the following equation known as the Tauc plot [56]:

$$\alpha h\nu = (h\nu - E_g)^n$$

where n is an exponent, ν is the frequency of the incident radiation, h is the Plank′s constant, and Eg is the optical energy gap of the material. The exponent n can take the values 2, 3, 1/2 and 3/2 for indirect allowed, indirect forbidden, direct allowed and direct forbidden transitions, respectively [57]. The inset in Fig. 8 presents the variation of $(\alpha h\nu)^2$ versus $h\nu$ for VO_2(B) nanoplates and nanorods. The optical band gap (Eg) can be calculated by extrapolating the linear portion of the plot of $(\alpha h\nu)^2$ versus $h\nu$ to $\alpha = 0$. The Eg values of VO_2(B)

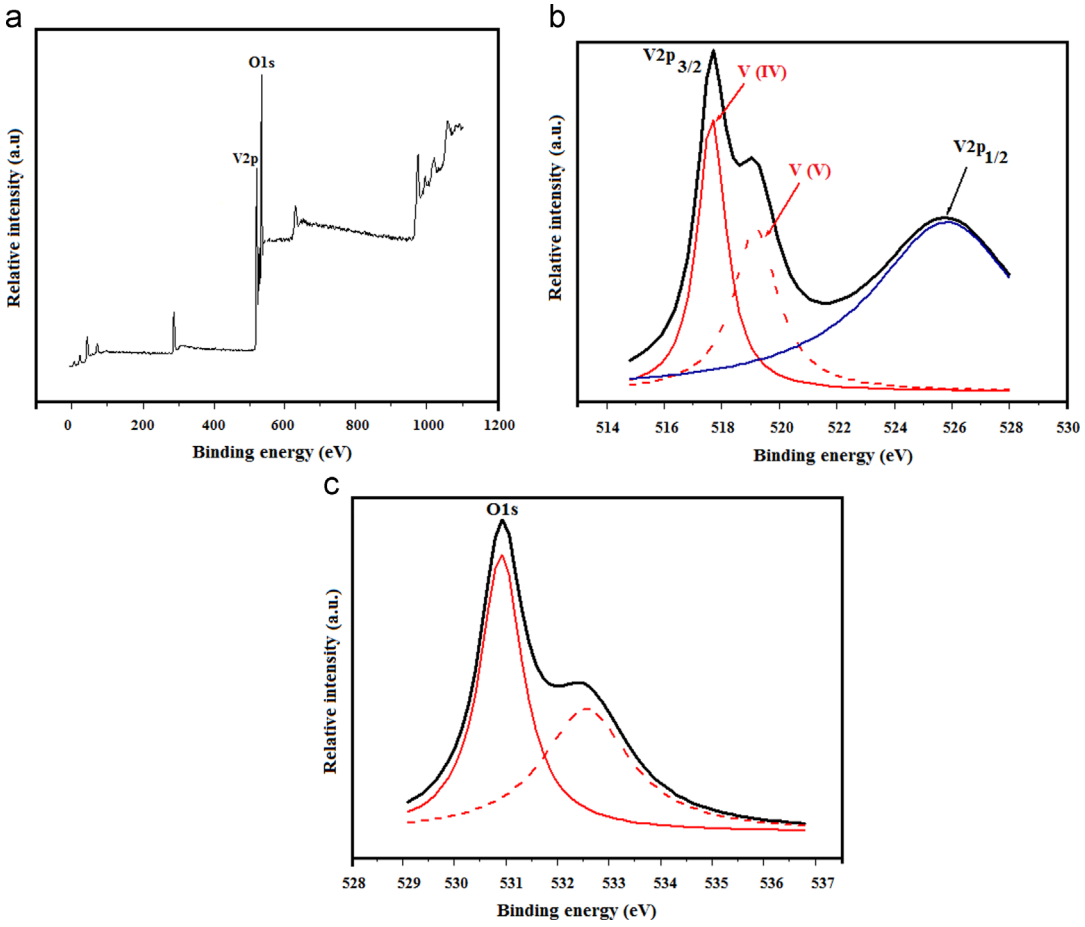

Fig. 7. The survey XPS spectrum of VO_2(B) nanorods (a) and core level spectra of V_{2p} (b), and O_{1s} (c).

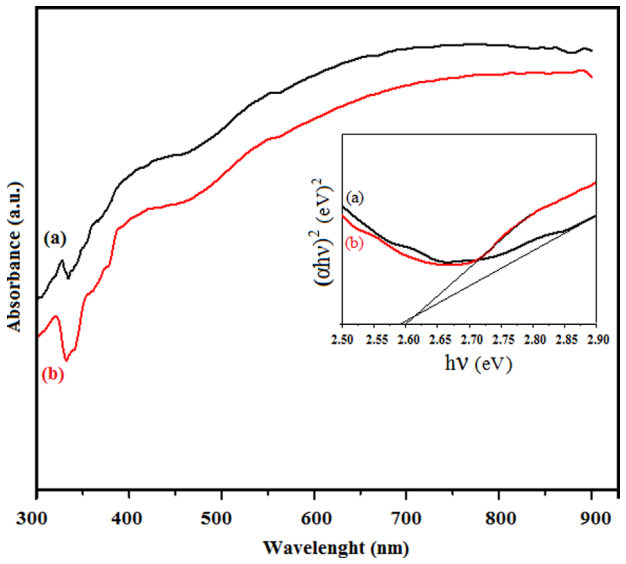

Fig. 8. UV–visible absorption spectra and the $(\alpha h\nu)^2$ vs. hν plot (insert) of VO_2(B) nanoplates (a) and nanorods (b).

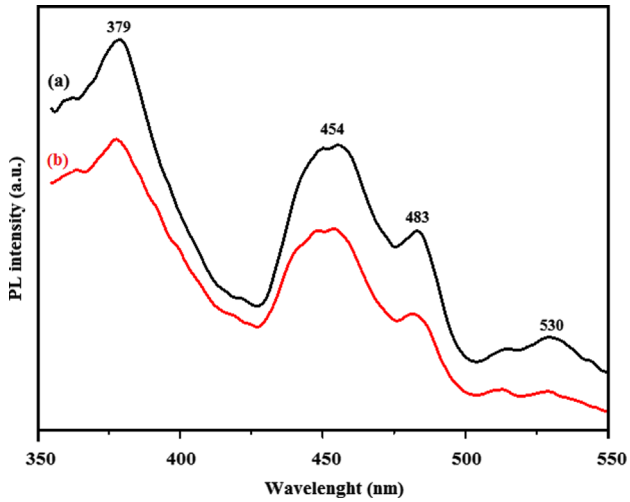

Fig. 9. Room temperature Photoluminescence spectra of VO_2(B) nanoplates (a) and nanorods (b).

nanoplates and nanorods are found to be 2.59 and 2.60 eV, respectively. The optical band gap of the sample can be attributed to direct transition from occupied 2p bands of oxygen to unoccupied 3d bands of vanadium in VO_2(B).

Photoluminescence (PL) property can explain the nature of the intrinsic defect in VO_2(B) because the energy levels associate with the defects populating the large band gap of the material and producing radiative emissions at different wavelengths. Fig. 9 shows the PL spectra of the VO_2(B)

Table 1
The BET surface area, pore volume and average pore size analysis of VO_2(B) nanoplates and nanorods.

	S_{BET} ($m^2\ g^{-1}$)	V_{por} ($cm^3\ g^{-1}$)	d_{por} (Å)
Nanoplates	23	0.040	45
Nanorods	12	0.060	93

nanoplates and nanorods under the excitation of the 325 nm Xe lamp. However, there was no obvious difference can be found in the emission spectra among VO_2(B) samples. The morphology changed from plate-like to rod-like only caused an increasing in the photoluminescent peak intensity; but the positions of the peaks hardly altered. In fact, the spectra reveal that the samples consist of several bands with a very broad band in the region 350–550 nm. Indeed, the peak at 379 nm may be assigned to free-excition emission [58,59]. However, the luminescent mechanism at 454 nm was attributed to the electric charge transfer, corresponding to the weak energy of V═O bond [60]. Besides, the shoulder peaks at 483 nm and 530 nm may be caused by defect energy gap [59,61].

3.7. Nitrogen adsorption

The Table 1 shows the specific BET surface area (S_{BET}), pore volume (V_{por}) and average pore size (d_{por}) of nanoplates and nanorods. Indeed, the specific BET surface area values of VO_2(B) nanoplates and nanorods are found to be 23 and 12 $m^2\ g^{-1}$, respectively. Liu et al. prepared hollow spherical VO_2(B) material by the hydrothermal method, its specific BET surface area reaches 13.02 $m^2\ g^{-1}$ [62]. It is known to all that many chemical and physical properties of products deeply depend on both initial material size and synthetic method. Moreover, N_2 adsorption–desorption isotherms of the samples exhibit IV-type hysteresis loops. In fact, IV-type is usually observed with rigid bulk particles having a uniform sizes [63]. It is worthwhile to be noted that these mesopores are very important and a key for offering more electroactive sites for an easy access of the ions adsorption in the electrolyte improving therefore the utilization of active materials during the charge–discharge process. These materials are promising for chemical and energy-related applications such as catalysts and electrochemical device.

3.8. Electrochemical characterization

It was reported that the electrochemical properties of the electrode materials are influenced by many factors such as instinctive structure, morphology, and preparation processes [64]. Cyclic voltammetric curves shown in Figs. 10 and 11 were recorded for the 1st and the 50th cycles at room temperature with a scan rate of 50 mV/s in the range −0.4–1 V in 1 mol dm^{-3} $LiClO_4$ aqueous solution and propylene carbonate solution, respectively. In both media the CV data are consistent with good stability of the as-prepared crystalline VO_2(B) nanorods coated films. In fact, in aqueous solutions one process is observed and, after several voltammetric cycles,

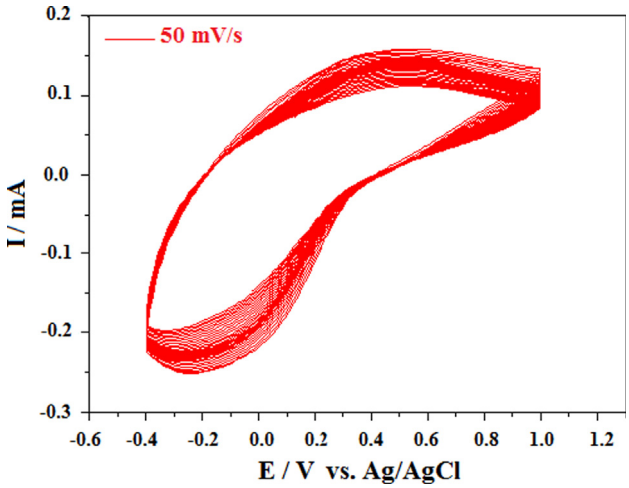

Fig. 10. Cyclic voltammetric responses of VO_2(B) nanorods deposited on ITO-covered glass slide. Voltammograms were recorded at 50 mV/s scan rate from 1st to 50th cycles and at room temperature in 1 mol dm^{-3} $LiClO_4$ aqueous solution.

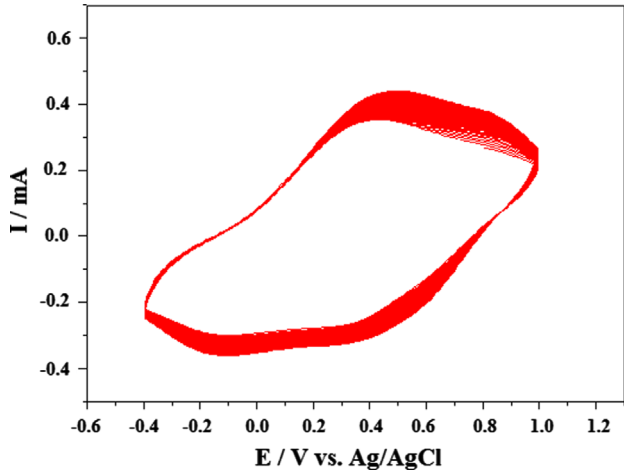

Fig. 11. Cyclic voltammetric responses of m–VO_2(B) nanorods deposited on ITO-covered glass slide. Voltammograms were recorded at 50 mV/s scan rate from 1st to 50th cycles and at room temperature in 1 mol dm^{-3} $LiClO_4$ propylene carbonate solution.

the voltammetric responses remain unchanged (Fig. 10). The voltammograms show the presence of a single redox process. The cathodic and anodic peaks at −0.20 V and 0.40 V can be attributed to intercalation/deintercalation process of Li^+ ions in the sample, which mainly corresponds to the reduction of V^{4+} to V^{3+} and the oxidation of V^{3+} to V^{4+}, respectively. It should be noted that the cyclic voltammetric responses recorded at low scan rates always reveal the presence of only redox

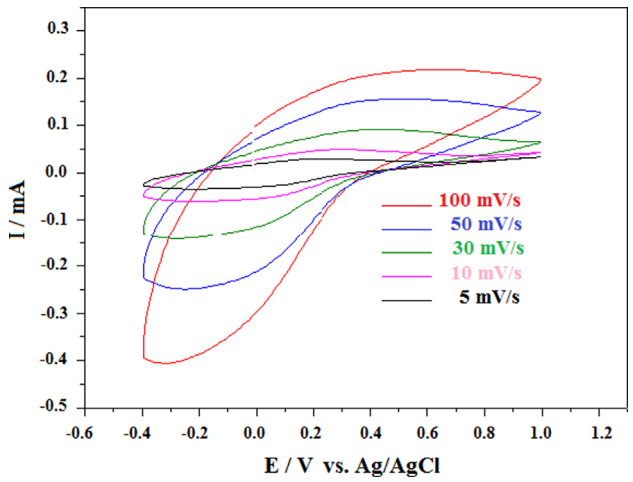

Fig. 12. Cyclic voltammetric curves of the 1st cycle responses of VO_2(B) nanorods deposited on ITO-covered glass slide recorded at different scan rates (5, 10, 30, 50 and 100 mV/s) at room temperature in 1 mol dm^{-3} $LiClO_4$ aqueous solution.

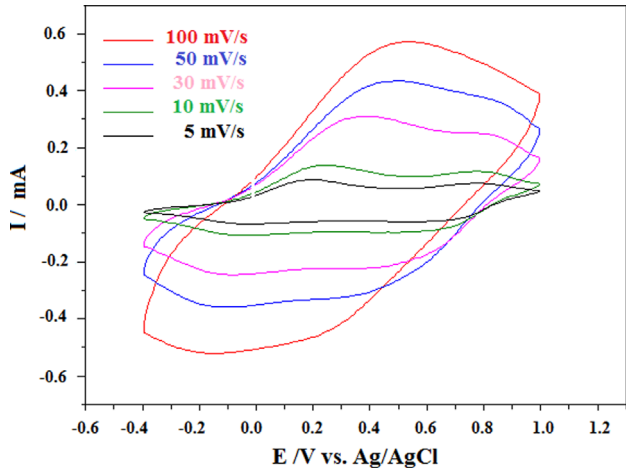

Fig. 13. Cyclic voltammetric curves of the 1st cycle responses of monoclinic-VO_2(B) nanorods deposited on ITO-covered glass slide recorded at different scan rates (5, 10, 30, 50, 100 mV/s) at room temperature in 1 mol dm^{-3} $LiClO_4$ propylene carbonate solution.

process (Fig. 12). However, in organic media, two redox processes are observed and, after several voltammetric cycles, the voltammetric responses remain unchanged. Indeed, the sample shows two cathodic peaks at 0.28 V and −0.10 V during the process of Li^+ ion intercalation which corresponds to two different intercalation stages. The corresponding anodic peaks at 0.43 V and 0.83 V are assigned to the deintercalation of Li^+ ion [65]. This fact may reflect the importance of scan rates used because, in the present work, fairly low scan rate was applied in comparison to the value of 100 mV/s used earlier [66]. Indeed, when the scan rate has been decreased to 5 mV/s (Fig. 13), the system's voltammetric characteristic features are more evident thus indicating the importance of dynamics of lithium intercalation/deintercalation occurring in the material to provide electroneutrality. Obviously, the cathodic and anodic peak currents increased simultaneously

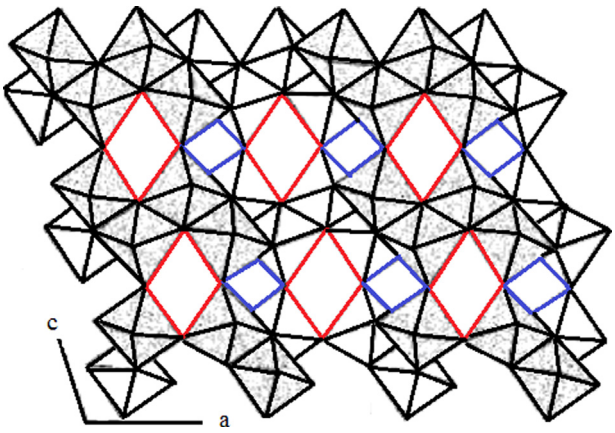

Fig. 14. Arrangement of VO_6 octahedra in VO_2(B). Small and large open cavities refer to small and large rectangular tunnel cavities, respectively.

with the increment of scan rate. It can be observed that the scan rate affected the position of the redox peaks. This phenomenon indicates the dynamics of the lithium intercalation/deintercalation occurring in the material to provide electroneutrality. Changes in kinetics of lithium intercalation/deintercalation reflect differences in morphology at the nanoscale, namely due to the presence of two types of one-dimensional tunnel cavities where the Li^+ cation intercalation/ deintercalation occurs. It is noteworthy that in the arrangement of VO_6 octahedra, the VO_2(B) structure (Fig. 14) exhibits large rectangular tunnel cavities where V atoms can be easily reached by Li^+ cations during redox processes. On the other hand, the same VO_2(B) structure is characterized by smaller secondary rectangular tunnel cavities capable of limiting migration of Li^+ cations during the system's redox processes. The fact that we observe mainly two redox processes is probably due to the small difference in the lithium ions insertion in the rectangular-cavities of VO_2(B) nanorods. This observation may be correlated with the fact that the intercalation/deintercalation processes of Li^+ is more rapid in aqueous solution because this cation is better solvated than in more viscous propylene carbonate. Consequently, the aqueous medium seems to facilitate the Li^+ intercalation/deintercalation process. Moreover, when the films of VO_2(B) nanorods deposited on ITO electrode have been studied in propylene carbonate containing $NaClO_4$ as electrolyte instead of $LiClO_4$ (Figs. 15 and 16), the observed electrochemical currents have largely increased upon medium transfer from Na^+ to Li^+ containing electrolyte. This observation indicates that intercalation/deintercalation processes involving Na^+ are less effective and more difficult in comparison to those with Li^+ cations. It should be remembered that the Van der Waals radius of Na^+ is larger than that of Li^+ cation. In addition the tunnel size (4.984 Å × 3.281 Å) of VO_2 (B) is considerably larger than the diameter of Li-ion (1.36 Å) and Na^+ (1.75 Å) [67]. In view of our data and previous results, it is reasonable to expect that the diffusion process of cations is mainly controlled by the sizes of large cavities; and to lower extent, by the small secondary rectangular tunnel cavities. The excellent stability of VO_2(B) nanocrystallites makes it an

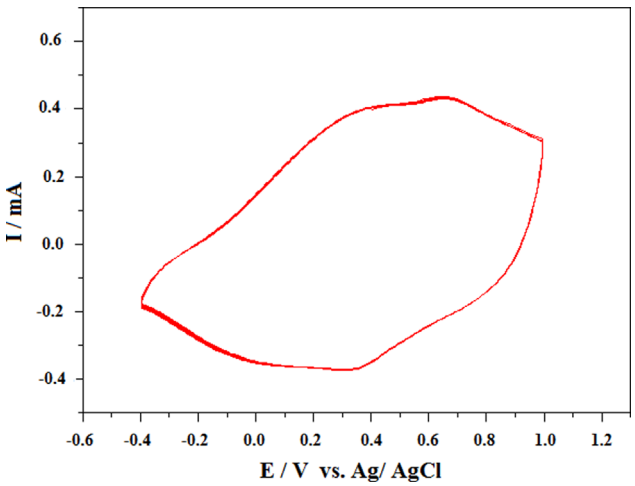

Fig. 15. Cyclic voltammetric responses of VO_2(B) nanorods deposited on ITO-covered glass slide. Voltammograms were recorded at 50 mV/s scan rate from 1st to 50th cycles and at room temperature in 1 mol dm^{-3} $NaClO_4$ propylene carbonate solution.

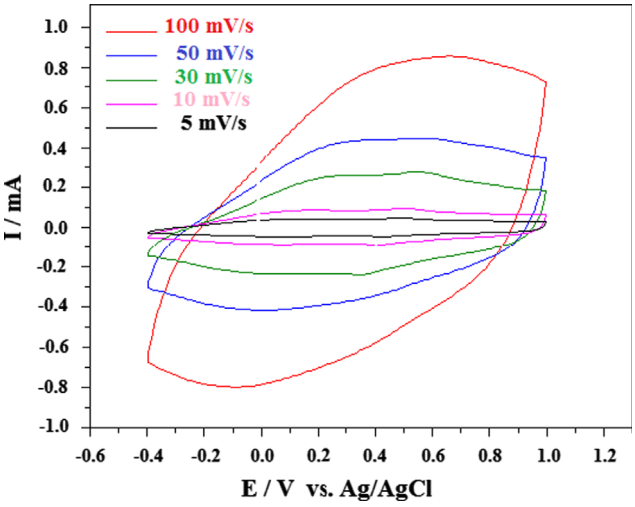

Fig. 16. Cyclic voltammetric curves of the 1st cycle responses of VO_2(B) nanorods deposited on ITO-covered glass slide recorded at different scan rates (5, 10, 30, 50, 100 mV/s) at room temperature in 1 mol dm^{-3} $NaClO_4$ propylene carbonate solution.

interesting possible future electrode for rechargeable lithium cell.

4. Conclusion

Mesoporous VO_2(B) nanoplates and nanorods were synthesized hydrothermally via a simple and elegant route from the mixture of V_2O_5 and HO–$(CH_2)_n$–OH (with $n=3$ and 5) under soft conditions. In fact, the structure directing agents played an important role in the structure and the morphology of the final products. Electrochemical measurements were carried out on thin films deposited on ITO-modified glass electrodes and revealed reversible redox behavior corresponding to partial reduction of vanadium oxide, with charge–discharge cycling corresponding to the reversible intercalation/deintercalation of lithium ions into the crystal lattice of the VO_2(B) nanorods. The VO_2(B) crystal structure exhibited two different tunnel cavities leading to two successive redox processes and, consequently to two different Li^+-ion intercalation/deintercalation processes. The rapid diffusion process occurred in the large rectangular tunnel cavities where V atoms could be easily be reached by Li^+ cations during redox processes; whereas, the slowest diffusion process occurred in the smaller secondary rectangular tunnel cavities. This result was supported by the observation of lower cyclic voltammetric currents measured in propylene carbonate medium when $NaClO_4$ was used instead of $LiClO_4$ as the electrolytic salt. Further, higher current was measured for the same material and the same electrolytic salt when the aqueous medium was used instead of the organic propylene carbonate solvent. All these results indicate that the resulting VO_2(B) nanorods are promising cathode materials in lithium-ion batteries.

References

[1] H. Qiao, X. Zhu, Z. Zheng, L. Liu, L. Zhang, Synthesis of $V_3O_7 \cdot H_2O$ nanobelts as cathode for lithium-ion batteries, Electrochemical Communication 8 (2006) 21–26.

[2] G. Nagaraju, G.T. Chandrappa, Solution phase synthesis of $Na_{0.28}V_2O_5$ nanobelts into nanorings and the electrochemical performance in Li battery, Materials Research Bulletin 47 (2012) 3216–3223.

[3] A. Umar, A. Al-Hajry, Y.B. Hahn, D.H. Kim, Rapid synthesis and dye-sensitized solar cell applications of hexagonal-shaped ZnO nanorods, Electrochimica Acta 54 (2009) 5358–5362.

[4] Y. Zhang, X. Liu, G. Xie, L. Yu, S. Yi, M. Hu, C. Huang, Hydrothermal synthesis, characterization, formation mechanism and electrochemical property of $V_3O_7 \cdot H_2O$ single-crystal nanobelts, Materials Science and Engineering: B 175 (2010) 164–171.

[5] M. Zeng, H. Yin, Ke Yu, Synthesis of V_2O_5 nanostructures with various morphologies and their electrochemical and field-emission properties, Chemical Engineering Journal 188 (2012) 64–70.

[6] H. Peng, W. Wu, C. Zhang, G. Li, K. Chen, Synthesis and electrochemical properties of $Ag_{0.333}V_2O_5$–V_2O_5 core–shell nanobelts for rechargeable lithium batteries, Materials Letters 65 (2011) 3436–3439.

[7] Ch.V.S. Reddy, E.H.W. Jr, S.A.W. Sr, Q.L. Williams, R.R. Kalluru, Synthesis of VO_2(B) nanorods for Li battery application, Current Applied Physics 9 (2009) 1195–1198.

[8] B. Jeon, C. Ko, A.C.T. Duin, S. Ramanathan, Chemical stability and surface stoichiometry of vanadium oxide phases studied by reactive molecular dynamics simulations, Surface Science 606 (2012) 516–522.

[9] M. Womes, T. Cholley, F. Le Peltier, S. Morin, B. Didillon, N. Szydlowski-Schildknecht, Study of the reaction mechanisms between $Pt(acac)_2$ and alumina surface sites Application to a new refilling technique for the controlled variation of the particle size of Pt/Al_2O_3 catalysts, Applied Catalysis A: General 283 (2005) 9–22.

[10] W. Li, J. Liu, C. Yan, The electrochemical catalytic activity of single-walled carbon nanotubes towards VO_2^+/VO^{2+} and V^{3+}/V^{2+} redox pairs for an all vanadium redox flow battery, Electrochimica Acta 79 (2012) 102–108.

[11] Y. Wang, G. Cao, Synthesis and enhanced intercalation properties of nanostructured vanadium oxides, Chemistry of Materials 18 (2006) 2787–2804.

[12] Z. Chen, S. Gao, L. Jian, M. Wei, K. Wei, Flexible free-standing VO_2(B) nanobelt films as additive-free cathode for lithium–ion batteries, Materials Chemistry and Physics 121 (2010) 254–258.

[13] W. Jiang, J. Ni, K. Yu, Z. Zhu, Hydrothermal synthesis and electrochemical characterization of VO_2(B) with controlled crystal structures, Applied Surface Science 257 (2011) 3253–3258.

[14] J.H Song, H.J. Parka, K.J. Kima, Y.N. Jo, J.S. Kima, Y.U. Jeong, Y.J. Kim, Electrochemical characteristics of lithium vanadate, $Li_{1+x}VO_2$, new anode materials for lithium ion batteries, Journal of Power Sources 195 (2010) 6157–6161.
[15] K.H. Chang, C.C. Hu, $H_2V_3O_8$ single-crystal nanobelts: hydrothermal preparation and formation mechanism, Acta Materialia 55 (2007) 6192–6197.
[16] M.M. Rahman, J.Z. Wang, N.H. Idris, Z. Chen, H. Liu, Enhanced lithium storage in a VO_2(B)-multiwall carbon nanotube microsheet composite prepared via an in situ hydrothermal process, Electrochimica Acta 56 (2010) 693–699.
[17] S. Gao, Z. Chen, M. Wei, K. Wei, H. Zhoud, Single crystal nanobelts of V_3O_7. H_2O: a lithium intercalation host with a large capacity, Electrochimica Acta 54 (2009) 1115–1118.
[18] Y. Zhang, C. Chen, W. Wu, F. Niu, X. Liu, Y. Zhong, Y. Cao, X. Liu, C. Huang, Facile hydrothermal synthesis of vanadium oxides nanobelts by ethanol reduction of peroxovanadium complexes, Ceramics International 39 (2013) 129–141.
[19] F.J. Morin, Oxides which show a metal-to-insulator transition at the neel temperature, Physical Review Letters 3 (1959) 34–36.
[20] X. Chen, Q. Lv, Theoretical analysis on the switching speed and driving power dissipation for optical switch based on VO_2 thin film, Optik 124 (2013) 579–582.
[21] Y. Zhang, M. Fan, F. Niu, W. Wu, C. Huang, X. Liu, H. Li, X. Liu, Belt-like VO_2(M) with a rectangular cross section: a new route to prepare, the phase transition and the optical switching properties, Current Applied Physics 12 (2012) 875–879.
[22] N. Li, W. Huang, Q. Shi, Y. Zhang, L. Song, A CTAB-assisted hydrothermal synthesis of VO_2(B) nanostructures for lithium–ion battery application, Ceramics International 39 (2013) 6199–6206.
[23] A.M. Kannan, A. Manthiram, Synthesis and electrochemical evaluation of high capacity nanostructured VO_2 cathodes, Solid State Ionics 159 (2003) 265–271.
[24] G.T. Chandrappa, P. Chithaiah, S. Ashoka, J. Livage, Morphological evolution of $(NH_4)_{0.5}V_2O_5 \cdot mH_2O$ fibers into belts, triangles, and rings, Inorganic Chemistry 50 (2011) 7421–7428.
[25] G.T. Chandrappa, N. Steunou, J. Livage, Materials chemistry: macroporous crystalline vanadium oxide foam, Nature 416 (2002) 702–703.
[26] L. Soltane, F. Sediri, N. Gharbi, Hydrothermal synthesis of mesoporous VO_2. 1/2(H_2O) nanosheets and study of their electrical properties, Materials Research Bulletin 47 (2012) 1615–1620.
[27] M.K. Chine, F. Sediri, N. Gharbi, Solvothermal synthesis of V_4O_9 flake-like morphology and its photocatalytic application in the degradation of methylene blue, Materials Research Bulletin 47 (2012) 3422–3426.
[28] J. Ma, Q. Wu, Y. Chen, An oxides-hydrothermal approach from bulky V_2O_5 powder to V_3O_7. H_2O nanoribbons or V_3O_7 nanoflowers in various ethanol/water mixed solvent, Materials Research Bulletin 44 (2009) 1142–1147.
[29] F. Sediri, N. Gharbi, Controlled hydrothermal synthesis of VO_2(B) nanobelts, Materials Letters 63 (2009) 15–18.
[30] S. Salmaoui, F. Sediri, N. Gharbi, Characterization of h-WO_3 nanorods synthesized by hydrothermal process, Polyhedron 29 (2010) 1771–1775.
[31] F. Sediri, N. Gharbi, From crystalline V_2O_5 to nanostructured vanadium oxides using aromatic amines as templates, Journal of Physics and Chemistry of Solids 68 (2007) 1821–1829.
[32] L. Bouhedja, N. Stenou, J. Maquet, J. Livage, Synthesis of polyoxovanadates from aqueous solutions, Journal of Solid State Chemistry 162 (2001) 315–321.
[33] N. Ganganagappa, A. Siddaramanna, One step synthesis of monoclinic VO_2(B) bundles of nanorods: cathode for Li ion battery, Materials Characterization 68 (2012) 58–62.
[34] F. Sediri, N. Gharbi, Nanorod B phase VO_2 obtained by using benzylamine as a reducing agent, Materials Science and Engineering: B 139 (2007) 114–117.
[35] G. Nagaraju, G.T. Chandrappa, Solution phase synthesis of $Na_{0.28}V_2O_5$ nanobelts into nanorings and the electrochemical performance in Li battery, Materials Research Bulletin 47 (2012) 3216–3223.
[36] Y. Zhang, J. Zhang, Y. Zhong, L. Yu, Y. Denga, C. Huang, X. Liu, Direct fabrication of organic carbon coated VO_2(B) (VO_2(B)@C) core–shell structured nanobelts by one step hydrothermal route and its formation mechanism, Applied Surface Science 263 (2012) 124–131.
[37] Ch.V. Subba Reddy, E.H.W. Jr., S.A.W. Sr, Q.L. Williams, R.R. Kalluru, Synthesis of VO_2(B) nanorods for Li battery application, Current Applied Physics 9 (2009) 1195–1198.
[38] R. Li, C.Y. Liu, VO_2(B) nanospheres: hydrothermal synthesis and electrochemical properties, Materials Research Bulletin 45 (2010) 688–692.
[39] S. Santangelo, G. Messina, G. Faggio, M.-G. Willinger, N. Pinna, A. Donato, A. Arena, N. Donato, G. Neri, Micro-Raman investigation of vanadium–oxide coated tubular carbon nanofibers for gas-sensing applications, Diamond and Related Materials 19 (2010) 590–594.
[40] X.J. Wang, H.D. Li, Y.J. Fei, X. Wang, Y.Y. Xiong, Y.X. Nie, K. A. Feng, XRD Raman study of vanadium oxide thin films deposited on fused silica substrates by RF magnetron sputtering, Applied Surface Science. 177 (2001) 8–14.
[41] S-H. Lee, H.M. Cheong, M.J. Seong, P. Liu, C.E. Tracy, A. Mascarenhas, J.R. Pitts, S.K. Deb, Raman spectroscopic studies of amorphous vanadium oxide thin films, Solid State Ionics 165 (2003) 111–116.
[42] W. Chen, L. Mai, J. Peng, Q. Xu, Q. Zhu, Raman spectroscopic study of vanadium oxide nanotubes, Journal of Solid State Chemistry 177 (2004) 377–379.
[43] N. Rama, M.S.R. Rao, Synthesis and study of electrical and magnetic properties of vanadium oxide micro and nanosized rods grown using pulsed laser deposition technique, Solid State Communication 150 (2010) 1041–1044.
[44] L. Soltane, F. Sediri, Hydrothermal synthesis, characterization and electrical investigation of poly (para-phenylenediamine)/vanadium oxide nanocomposite nanosheets, Materials Science and Engineering: B 178 (2013) 502–510.
[45] C. Julien, G.A. Nazri, O. Bergstrom, Raman Scattering Studies of Microcrystalline V_6O_{13}, solid state physics 201 (1997) 319–326.
[46] Y. Wang, Z. Zhang, Synthesis and field emission property of VO_2 nanorods with a body-centered-cubic structure, Physica E 41 (2009) 548–551.
[47] S. Ji, F. Zhang, P. Jin, Selective formation of VO_2(A) orVO_2(R) polymorph by controlling the hydrothermal pressure, Journal of Solid State Chemistry 184 (2011) 2285–2292.
[48] X. Liu, G. Xie, C. Huang, Q. Xu, Y. Zhang, Y. Luo, A facile method for preparing VO_2 Nanobelts, Materials Letters 62 (2008) 1878–1880.
[49] B.T. Sone, R. Benoit, S. Zongo, R. Bucher, M. Maaza, Time-based investigation of the growth of VO_2(B) micro- and nano-structures on vanadium by hydrothermal synthesis, Materials Chemistry and Physics 136 (2012) 358–370.
[50] C.J. Cui, G.M. Wu, J. Shen, B. Zhou, Z.H. Zhang, H.Y. Yang, S.F. She, Synthesis and electrochemical performance of lithium vanadium oxide nanotubes as cathodes for rechargeable lithium-ion batteries, Electrochimica Acta 55 (2010) 2536–2541.
[51] V. Naydenov, L. Tosheva, J. Sterte, Spherical silica macrostructures containing vanadium and tungsten oxides assembled by the resin templating method, Microporous and Mesoporous Materials 55 (2002) 253–263.
[52] W. Ding, G.D. Meitzner, D.O. Marler, E. Iglesia, Synthesis, structural characterization, and catalytic properties of tungsten-exchanged H-ZSM5, Journal of Physical Chemistry B 105 (2001) 3928–3936.
[53] R. Huang, Y. Shen, L. Zhao, M. Yan, Advance effect of hydrothermal temperature on structure and photochromic properties of WO_3 powder, Powder Technology 23 (2012) 211–214.
[54] J. Kornatowski, B. Wichterlová, J. Jirkovsky, E. Löffler, W. Pilz, Spectroscopic studies of vanadium-substituted zeolitic silicates of MFI topology, Journal of the Chemical Society, Faraday Transactions 92 (1996) 1067–1078.
[55] M. Schrami-Marth, A. Wokaun, M. Pohl, H.-L. Krauss, Spectroscopic investigation of the structure of silica-supported vanadium oxide catalysts at submonolayer coverages, Journal of the Chemical Society, Faraday Transactions 87 (1991) 2635–2646.

[56] J. Tauc, R. Grigorovici, A. Vancu, Optical properties and electronic structure of amorphous germanium, Solid State Phyics (B) 15 (1966) 627–637.
[57] G.A. Khan, C.A. Hogarth, Optical absorption spectra of evaporated V2O5 and co-evaporated V_2O_5/B_2O_3 thin films, Journal of Materials Science 26 (1991) 412–416.
[58] J. Xu, C. Hua, Y. Xi, C. Peng, B. Wan, X. He, Synthesis, photoluminescence and magnetic properties of barium vanadate nanoflowers, Materials Research Bulletin 46 (2011) 946–950.
[59] C. Niu, C. Han, Y. Zhao, X. Tian, W. Guo, Y. Gu, L. Mai, Synthesis and optical property of size-tunable vanadium oxide nano-dandelions, Journal of Nanoscience Letters 3 (2013) 27.
[60] M. Anpo, I. Tanahashi, Y. Kubokawa, Photoluminescence and photoreduction of V_2O_5 supported on porous vycor glass, Journal of Physical Chemistry 84 (1980) 3440–3443.
[61] M. Kang, E. Oh, I. Kim, S.W. Kim, J.W. Ryu, Y.G. Kim, Optical characteristics of amorphous V_2O_5 thin films colored by an excimer laser, Current Applied Physics 12 (2012) 489–493.
[62] H.M. Liu, Y.G. Wang, K.X. Wang, E. Hosono, H.S. Zhou, Design and synthesis of a novel nanothorn VO_2(B) hollow microsphere and their application in lithium–ion batteries, Journal of Materials Chemistry 19 (2009) 2835–2840.
[63] K.S.W. Sing, D.H. Everett, R.A.W. Haul, L. Moscou, R.A. Pierotti, J. Rouquerol, T. Siemieniewska, Reporting physisorption data for gas/solid systems with special reference to the determination of surface area and porosity, Pure and applied chemistry Chimie pure et appliquée 57 (1985) 603–619.
[64] M.K. Chine, F. Sediri, N. Gharbi, Hydrothermal Synthesis of V_3O_7 H_2O nanobelts and study of their electrochemical properties, Material Science Applications 2 (2011) 964–970.
[65] X. Zhou, G. Wu, G. Gao, C. Cui, H. Yang, J. Shen, B. Zhou, Z. Zhang, The synthesis, characterization and electrochemical properties of multi-wall carbon nanotube-induced vanadium oxide nanosheet composite as a novel cathode material for lithium ion batteries, Electrochimica Acta 74 (2012) 32–38.
[66] L. Liang, H. Liu, W. Yang, Fabrication of VO_2(B) hybrid with multi-walled carbon nanotubes to form a coaxial structure and its electrochemical capacitance performance, Journal of Alloys and Compounds 559 (2013) 167–173.
[67] J. Ni, W. Jiang, K. Yu, Y. Gao, Z. Zhu, Hydrothermal synthesis of VO_2(B) nanostructures and application in aqueous Li-ion battery, Electrochimica Acta 56 (2011) 2122–2126.